Journal of Materials Chemistry C

ROYAL SOCIETY OF CHEMISTRY

COMMUNICATION

View Article Online
View Journal | View Issue

Cite this: J. Mater. Chem. C, 2025, 13, 18631

Received 3rd June 2025,
Accepted 26th August 2025

DOI: 10.1039/d5tc02160j

rsc.li/materials-c

Ferromagnetic intercalated compounds $CrHf_xTe_2$ with a magnetocaloric effect and negative magnetoresistance

Kunqi Li,[ab] Xueyang Tu,[ab] Xuzhou Sun,[ab] Hui Bi,*[a] Yuqiang Fang*[c] and Fuqiang Huang *[c]

Intercalation in van der Waals materials enables novel structures and exotic properties. Herein, we have successfully synthesized two intercalated compounds $CrHf_xTe_2$ (x = 0.1, 1/3) *via* a flux method. $CrHf_{0.1}Te_2$ and $CrHf_{1/3}Te_2$ exhibit ferromagnetism with Curie temperatures of 234.9 K and 247.2 K under out-of-plane fields. The maximum magnetic entropy variation of $CrHf_{0.1}Te_2$ attains 2.85 J kg^{-1} K near 185 K, and the relative cooling power (216.6 J kg^{-1}) exceeds that of multiple van der Waals ferromagnets. Furthermore, negative magnetoresistances of −3.8% and −4.7% are respectively observed in $CrHf_{0.1}Te_2$ and $CrHf_{1/3}Te_2$. This work provides a strategy for designing new intercalation compounds promising for electronic and magnetic applications.

Introduction

Magnetic van der Waals (vdW) materials hold particular promise for nano-scale spintronics devices, magnetic sensors and magnetic refrigeration due to their inherent spin polarization, potential spin–orbit torque effect or intrinsic magnetocaloric effects.[1–4] In recent years, the discovery of novel vdW ferromagnets has provided an ideal platform for exploring exotic quantum states such as large tunneling magnetoresistances and magnetic skyrmions. For instance, ferromagnetic CrI_3 is characterized by an extremely robust tunnelling magnetoresistance (as large as 10 000%).[5] Moreover, chiral magnetic phases and Moire Skyrmions observed in twisted bilayer CrI_3 demonstrate the possibility of engineering nontrivial magnetic ground states.[6] However, the low T_C (61 K) of CrI_3 weakens its utilization potential in large-scale spintronic devices. Room-temperature ferromagnetic $CrTe_2$ is still gaining considerable research attention owing to its colossal anomalous Hall conductivity,[7] room-temperature in-plane anisotropic magnetoresistance[8] and many other unique physical properties.

The intercalation of atoms or molecules between the layers of vdW crystals can effectively adjust the electronic structure and interlayer interaction, thereby modifying the electronic and magnetic properties of the matrix. For TaS_2, magnetic atom intercalated $Fe_{0.25}TaS_2$ was confirmed to have long-range ferromagnetic order, a $\sqrt{3} \times \sqrt{3}$ superstructure, as well as an anomalous Hall effect.[9] In the $Cr_{1/3}TaS_2$ single crystal, the coupling of the strong spin–orbit interaction from TaS_2 and the chiral arrangement of Cr ions evokes a robust Dzyaloshinskii–Moriya interaction, hence forming chiral helimagnetism.[10] In terms of the intercalated $CrTe_2$ compound, $Cr_{1.25}Te_2$ was reported to present orthogonal ferromagnetism, featured by alternating in-plane and out-of-plane ferromagnetic layers coupled *via* antiferromagnetic exchange coupling.[11] As one of the 5d transition metals, the Hf atom possesses significantly strong spin–orbit coupling (SOC) effects. The intercalation of Hf atoms within vdW layered crystals probably enhances the SOC between the layers, thereby modifying the interlayer exchange interaction and the electronic bands, which is conducive to inducing novel electronic and magnetic properties.

In this work, we synthesized $CrHf_xTe_2$ (x = 0.1, 1/3) *via* a simple flux method. Similar to 1T $CrTe_2$, $CrHf_{0.1}Te_2$ crystallizes in a trigonal phase where each Cr atom is coordinated in a regular octahedron with Te atoms. In terms of magnetic properties, ferromagnetic $CrHf_{0.1}Te_2$ and $CrHf_{1/3}Te_2$ both exhibit perpendicular magnetic anisotropy due to significant SOC that retains the spin in an out-of-plane orientation. $CrHf_{0.1}Te_2$ demonstrates high Curie temperature (234.9 K) and large coercivity (691 Oe at 3 K), exceeding those of multiple Cr-based vdW ferromagnets. Along the easy magnetization axis, $CrHf_{0.1}Te_2$ displays the maximum magnetic entropy change of 2.85 J kg^{-1} K at approximately 185 K, and the relative cooling

[a] The State Key Laboratory of High-Performance Ceramics and Superfine Microstructure, Shanghai Institute of Ceramics, Chinese Academy of Sciences, Shanghai 200050, China. E-mail: bihui@mail.sic.ac.cn
[b] Center of Materials Science and Optoelectronics Engineering, University of Chinese Academy of Sciences, Beijing 100049, China
[c] State Key Lab of Metal Matrix Composites, School of Materials Science and Engineering, Zhangjiang Institute for Advanced Study, Shanghai Jiao Tong University, Shanghai 200240, China. E-mail: fangyuqiang@sjtu.edu.cn, huangfq@sjtu.edu.cn

power (216.6 J kg^{-1}) exceeds that of multiple vdW ferromagnets. Furthermore, intrinsic negative magnetoresistance exists in $CrHf_xTe_2$, rendering it a candidate for magnetic sensors. This study unveils a novel materials design strategy to synthesize intercalation compounds for advanced electronic and magnetic applications.

Results and discussion

$CrHf_xTe_2$ (x = 0.1, 1/3) crystals were prepared using CsI as the flux agent. CsI flux controls Hf intercalation in $CrTe_2$ as follows: first, Cs^+ ions temporarily intercalate into the interlayers in the molten state, enlarging the interlayer spacing and creating more diffusion channels for Hf atoms. Moreover, Hf dissolves in CsI and diffuses more rapidly than the solid-state diffusion, so that it is rapidly transported to the crystal surface. While $CrTe_2$ layers bear a weak negative charge, Hf^{4+} is positively charged. The ionic environment of CsI enhances electrostatic interactions, hence driving the migration of Hf^{4+} toward the interlayers. $CrHf_{0.1}Te_2$ crystallizes in the trigonal space group $P\bar{3}$ (No. 147). As shown in Fig. 1a, each Cr atom is coordinated by six Te atoms in a regular octahedron, and 10% Hf atoms are intercalated in the $CrTe_2$ layers. Fig. S1 (SI) reveals the lamellar morphologies of $CrHf_{0.1}Te_2$ and $CrHf_{1/3}Te_2$. Cr, Hf and Te elements are distributed homogeneously in the energy-dispersive X-ray spectroscopy (EDS) elemental mapping images, and Table S1 (SI) shows that the atomic proportion of Cr, Hf and Te is close to the stoichiometric ratio in $CrHf_xTe_2$.

The powder X-ray diffraction (XRD) pattern of $CrHf_{0.1}Te_2$ aligns well with the simulated diffraction peaks from the resolved single crystal structure through single-crystal X-ray diffraction (SC-XRD) (Fig. 1b). In contrast to $CrHf_{0.1}Te_2$, the diffraction peak of the (0 0 2) plane within $CrHf_{1/3}Te_2$ shifts from 2θ = 14.6° to 14.2°, indicating a slight increase in the crystal plane spacing (d). The crystallographic parameters of trigonal $CrHf_{0.1}Te_2$ are detailed in Tables S2–S6 ($a = b$ = 3.8907(6) Å, c = 6.1053(15) Å). For trigonal $CrHf_xTe_2$, the increase of d(002) means bigger c, the perpendicular parameters for $CrHf_{1/3}Te_2$. In addition, Raman spectroscopy was employed to probe diverse vibrational modes of chemical bonds. In Fig. 1c, two typical in-plane (E_g) and out-of-plane vibration modes (A_{1g}) are clearly found in the Raman spectra of $CrHf_xTe_2$. As the ratio of Hf element increases, both vibration peaks exhibit a slight blue shift (A_{1g} shifts from 121.3 cm^{-1} to 123.1 cm^{-1}, and E_g shifts from 139.6 cm^{-1} to 141.4 cm^{-1}). Compared with the A_{1g} (100.0 cm^{-1}) and E_g (134.1 cm^{-1}) modes of pure $CrTe_2$,[8] this kind of blue shift occurs due to increased interlayer coupling arising from intercalated atoms.[1] As the intercalated ratio of Hf elevates, the interlayer interaction, especially the SOC, gets enhanced, thereby modifying the magnetic or electric properties.

The chemical valences of Cr, Hf, and Te elements were investigated through X-ray photoelectron spectroscopy (XPS). Fig. 1d and e present the high-resolution XPS spectra for the Cr 2p, Te 3d and Hf 4f orbitals. The binding energies of the Cr $2p_{1/2}$ and Cr $2p_{3/2}$ peaks match well with the reference value for Cr^{3+} in Cr_2O_3 (Cr $2p_{1/2}$: 586.3 eV, Cr $2p_{3/2}$: 576.2 eV), confirming the +3 valence of Cr in the $CrHf_xTe_2$ systems.[12] The Hf 4f spectra both exhibit two pairs of characteristic peaks (18.8 eV and 17 eV for $CrHf_{0.1}Te_2$, 18.6 eV and 16.9 eV for $CrHf_{1/3}Te_2$), which correspond to the $4f_{5/2}$ and $4f_{7/2}$ orbitals of Hf^{4+}, respectively.[13]

The magnetic properties of the $CrHf_xTe_2$ crystals were examined through the vibrating sample magnetometer (VSM)

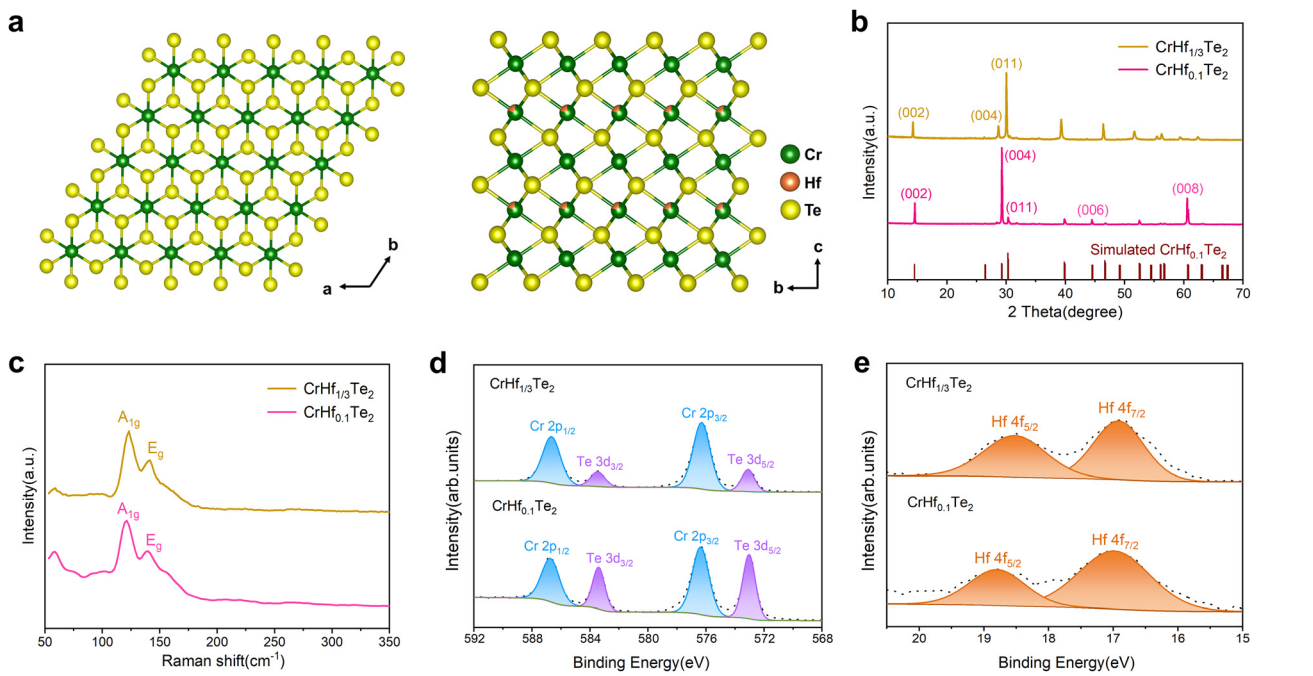

Fig. 1 (a) Crystal structure of trigonal $CrHf_{0.1}Te_2$ viewed from the c-axis and a-axis. (b) PXRD patterns. (c) Raman spectra. (d) and (e) High-resolution XPS spectra of Cr 2p, Te 3d and Hf 4f for $CrHf_xTe_2$ (x = 0.1, 1/3).

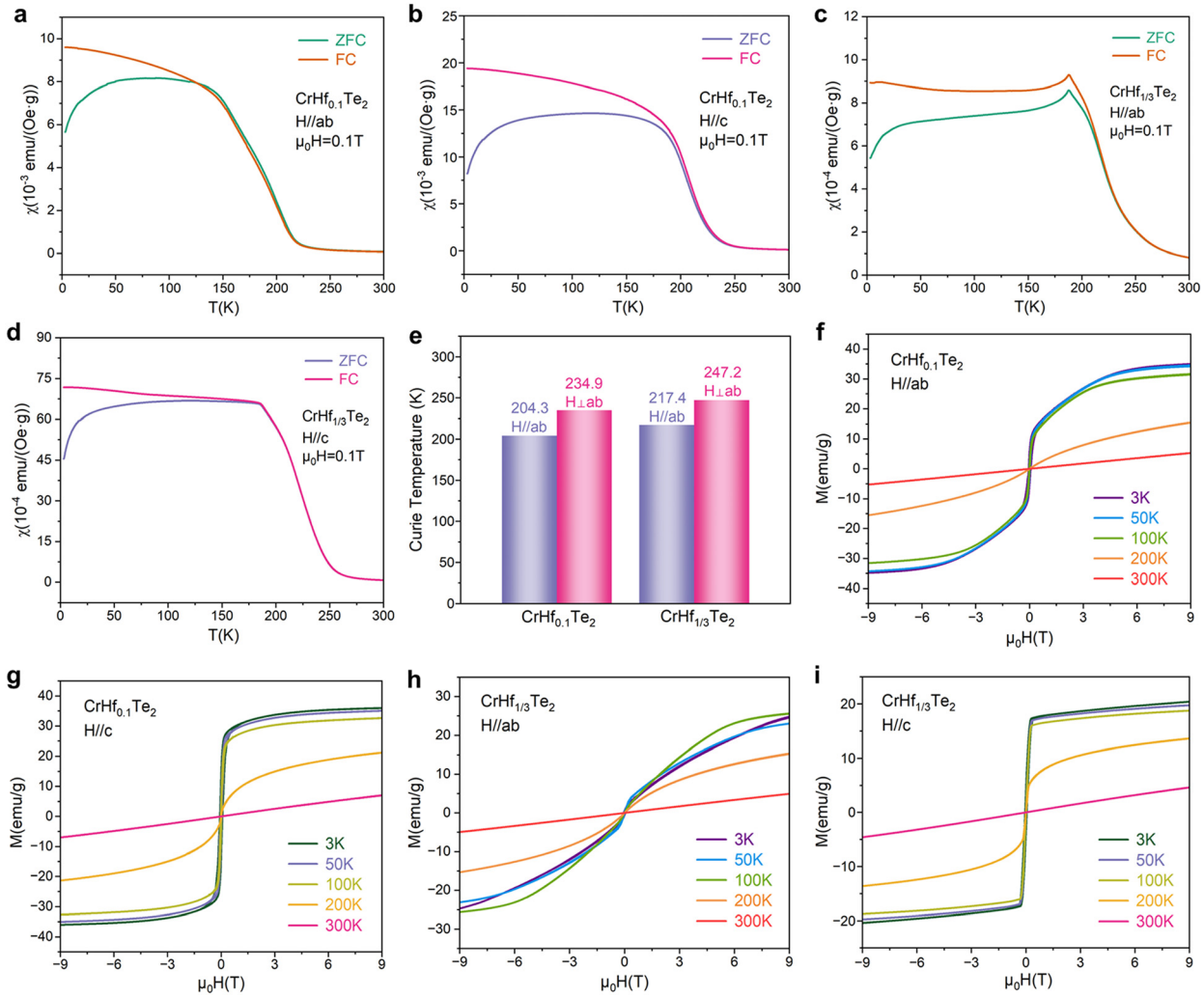

Fig. 2 (a) and (b) Temperature-dependent magnetization of $CrHf_{0.1}Te_2$ under a magnetic field parallel to the *ab*-plane and *c*-axis, respectively. (c) and (d) Temperature-dependent magnetization of $CrHf_{1/3}Te_2$ under a magnetic field parallel to the *ab*-plane and *c*-axis, respectively. (e) Calculated Curie temperatures of $CrHf_xTe_2$ along two different orientations. (f)–(i) Magnetic hysteresis loops of $CrHf_xTe_2$ for the H//*ab*-plane and H//*c*-axis.

module of a PPMS. Both measurement modes of zero-field-cooling (ZFC) and field-cooling (FC) were applied to obtain the temperature (T)-dependent magnetic susceptibilities (χ).

The χ–T curves demonstrate that the susceptibility values of both crystals are of 10^{-3} to 10^{-2} emu per (Oe·g) orders of magnitude under a 0.1 T magnetic field (Fig. 2a–d). For $CrHf_{1/3}Te_2$, the value of χ along the *c*-axis is approximately 8 times greater than that along the *ab*-plane. Based on the FC inverse susceptibility *versus* temperature (χ^{-1}–T) plots (Fig. S2, SI) and the Curie–Weiss law ($\chi = \chi_0 + C/(T - \theta_{CW})$, where θ_{CW} is equivalent to the Curie temperature (T_C) for ferromagnetic system), T_C was determined for these tested samples (Fig. 2e): when exerting the *in*-plane magnetic field (H//*ab*-plane), T_C of $CrHf_{0.1}Te_2$ and $CrHf_{1/3}Te_2$ attain 204.3 K and 217.4 K, respectively; under the out-of-plane field (H//*c*-axis), both $CrHf_{0.1}Te_2$ and $CrHf_{1/3}Te_2$ possess higher T_C (234.9 K and 247.2 K, respectively). Different magnetization intensities and Curie temperatures along two distinct orientations demonstrate magnetic anisotropy in the $CrHf_xTe_2$ crystals. Notably, the magnetization separations between the ZFC and FC processes below ~150 K are probably attributed to spin-glass-like irreversible thermomagnetic behavior under cryogenic conditions.[14] Furthermore, an abnormal AFM-like kink occurs in the in-plane χ–T curves of $CrHf_{1/3}Te_2$ (Fig. 2c). This phenomenon stems from the crossover from the pinning to the depinning of the magnetic moments.[15] In the ZFC process, the magnetic domains start to be pinned below the crossover temperature. As the applied field increases, the gained energy shifts the crossover temperature to a lower value.[16]

To further explore the field-dependent magnetization along the easy and hard orientations, we performed field-dependent magnetization curves from 3 K to 300 K, as shown in Fig. 2f–i. The hysteresis loops from −9 to 9 T at 3–200 K illustrate the typical ferromagnetic behavior in the $CrHf_xTe_2$ systems. In terms of $CrHf_{0.1}Te_2$ and $CrHf_{1/3}Te_2$, the easy magnetization axes are both parallel to the *c*-axis: magnetic saturation occurs at about 3 T and 1 T for $CrHf_{0.1}Te_2$ and $CrHf_{1/3}Te_2$ along the *c*-axis, which are smaller than 6 T and 8 T along the H//*ab*-plane direction. The measured saturated moments of $CrHf_{0.1}Te_2$ and $CrHf_{1/3}Te_2$ at 3 K along the *c*-axis reach 33.8 emu g^{-1} and

18.1 emu g^{-1}, respectively. Furthermore, large coercivities for both directions, as shown in Table S7 (SI), indicate the retentive ferromagnetism in both $CrHf_xTe_2$ crystals. In comparison with other reported Cr-based ferromagnetic materials (*e.g.* $CrBr_3$, CrI_3, $Cr_2Ge_2Te_6$, Cr_2Te_3 and Cr_5Te_8),[17–24] $CrHf_{0.1}Te_2$ demonstrates superior Curie temperature and coercivity (691 Oe at 3 K) at the easy magnetization orientation (Table S8, SI). Such a novel ferromagnetic crystal exhibits an excellent anti-demagnetization capability.

The perpendicular magnetic anisotropy in $CrHf_xTe_2$ arises from the SOC effect, which exists in both Te and Hf atoms. The p orbitals of Te tend to hybridize with the d orbitals of Cr, forming a strongly anisotropic electronic structure. While Cr 3d electrons form a ferromagnetic order through the itinerant mechanism, combined effects from SOC and the crystal field lead to the minimization of the out-of-plane exchange energy. Although pure $CrTe_2$ has an *in*-plane easy magnetization direction, the intercalation of Hf rotates the easy magnetization axis to the out-of-plane orientation, probably because such significant SOC from Hf atoms restricts the spin to the out-of-plane direction and minimizes the perpendicular magnetization energy.

The magnetocaloric effect in $CrHf_xTe_2$ systems is analyzed by the change of isothermal magnetic entropy ($\Delta S_M(T, H)$) which can be calculated from the isothermal field-dependent magnetization with a 4 K variation of temperature (Fig. 3a, b and Fig. S3a, b). $\Delta S_M(T, H)$ is defined as[25]

$$\Delta S_M(T,H) = \int_0^H [\partial S(T,H)/\partial H]\mathrm{d}H \quad (1)$$

According to the Maxwell equation $\partial S(T, H)/\partial H = \partial M(T, H)/\partial T$, $\Delta S_M(T, H)$ can be expressed as[25]

$$\Delta S_M(T,H) = \int_0^H [\partial S(T,H)/\partial T]\mathrm{d}H \quad (2)$$

For isothermal magnetization examined at small temperature intervals, $\Delta S_M(T, H)$ is approximately equivalent to[25]

$$\Delta S_M(T,H) = \left[\int_0^H M(T_{i+1},H) - \int_0^H M(T_i,H)\right] \Big/ (T_{i+1} - T_i) \quad (3)$$

Calculated $-\Delta S_M$ as a function of temperature under 1–9 T magnetic fields are shown in Fig. 3c, d and Fig. S3c, d. It is clear that the value of $-\Delta S_M$ at the same temperature elevates gradually with the external magnetic field increasing from 1 T to 9 T, and the maximum of $-\Delta S_M$ ($-\Delta S_M^{max}$) for the H//*c*-axis surpasses that for the H//*ab*-plane in $CrHf_xTe_2$ systems. For $CrHf_{0.1}Te_2$ and $CrHf_{1/3}Te_2$, $-\Delta S_M^{max}$ along the H//*c*-axis orientation reaches 2.85 J kg^{-1} K and 1.77 J kg^{-1} K, respectively. The relative cooling power (RCP), which determines the cooling efficiency, is expressed as RCP = $\Delta S_M^{max} \times \delta T_{FWHM}$ (δT_{FWHM} refers to the full width at half-maximum of the $-\Delta S_M(T, H)$ curve). Along the H//*c*-axis orientation, RCP is determined as 216.6 J kg^{-1} for $CrHf_{0.1}Te_2$ and 233.6 J kg^{-1} for $CrHf_{1/3}Te_2$. Although the magnetic entropy change of $CrHf_xTe_2$ is inferior to that of rare earth compounds (*e.g.* $TbScO_3$, ErNi, $EuCl_2$, $Er_{1-x}Tm_xGa$, Zr-doped $EuTiO_3$, *etc.*), the peaks of $-\Delta S_M$ are found only near the liquid hydrogen temperature (~20 K) for

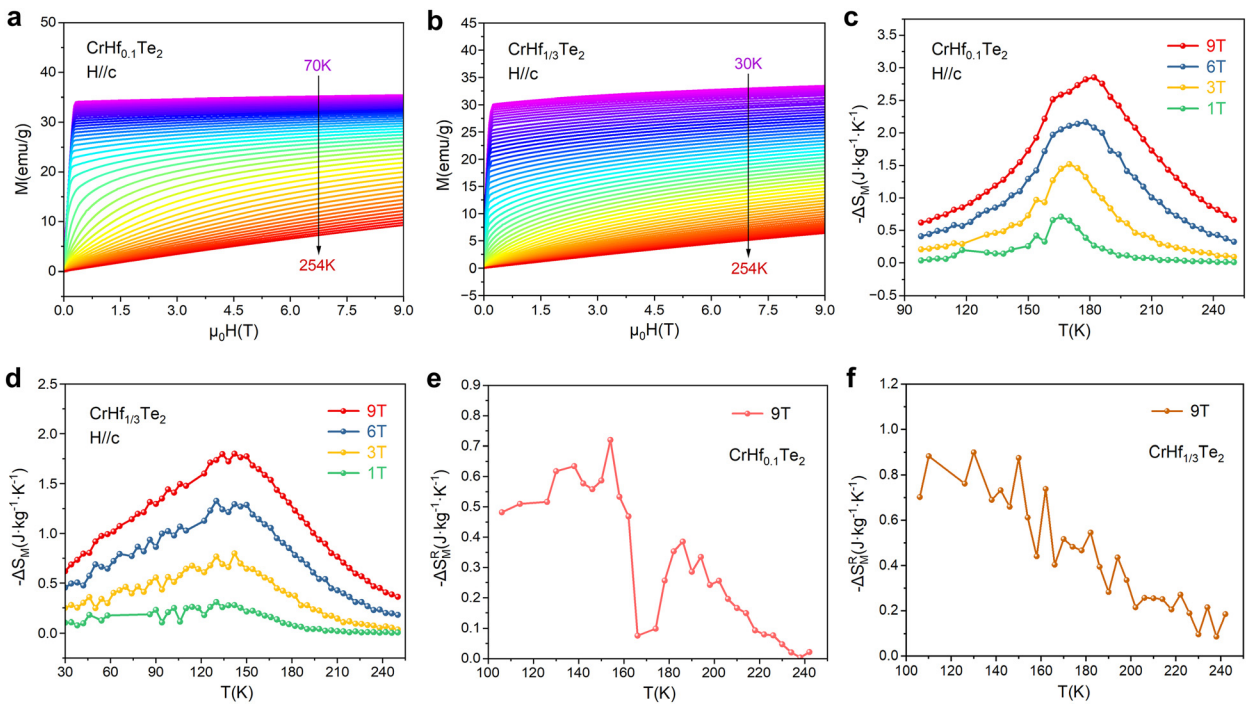

Fig. 3 (a) and (b) Isothermal field-dependent magnetization curves along the H//*c*-axis direction for $CrHf_{0.1}Te_2$ and $CrHf_{1/3}Te_2$, respectively. (c) and (d) Curves of $-\Delta S_M$ with temperature under a magnetic field parallel to the *c*-axis. (e) and (f) Rotating magnetic entropy changes of $CrHf_xTe_2$ obtained by rotating from the *c*-axis to the *ab*-plane.

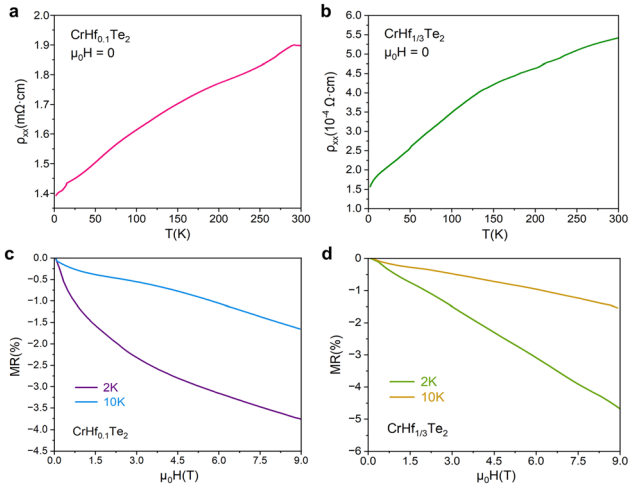

Fig. 4 (a) and (b) Temperature-dependent electrical resistivity (ρ_{xx}–T) curves. (c) and (d) Field-dependent magnetoresistance (MR–$\mu_0 H$) curves at 2 K and 10 K.

these compounds.[4,26–29] Table S9 reveals that the ΔS_M of $CrHf_{0.1}Te_2$ is comparable to that of reported vdW materials like VI_3, Fe_3GeTe_2 and $Cr_{1.15}Te_2$, but the RCP value significantly exceeds that of multiple vdW ferromagnets.[30–34] Notably, the peak of ΔS_M is located near 185 K, surpassing that of multiple vdW ferromagnets and rare-earth compounds.

The rotational magnetic entropy change (ΔS_M^R) is determined by rotating the field from the *c*-axis to the *ab*-plane:

$$\Delta S_M^R = \Delta S_M(T, H_c) - \Delta S_M(T, H_{ab}) \quad (4)$$

As depicted in Fig. 3e and f, all positive $-\Delta S_M^R$ further demonstrate the perpendicular magnetic anisotropy in $CrHf_xTe_2$. When applying a 9 T field, the peak of $-\Delta S_M^R$ attains 0.72 J kg^{-1} K for $CrHf_{0.1}Te_2$, and 0.9 J kg^{-1} K for $CrHf_{1/3}Te_2$. The higher concentration of intercalated Hf atoms probably strengthens the interlayer spin-orbital coupling, which tends to constrain the spin perpendicular to the *ab*-plane in $CrHf_xTe_2$, thereby enhancing the perpendicular magnetic anisotropy. As a result, the $-\Delta S_M^R$ peak value of $CrHf_{1/3}Te_2$ gets larger than that of $CrHf_{0.1}Te_2$ at a certain temperature and field.

To investigate the electrical transport characteristics, $CrHf_xTe_2$ flakes were connected into the measurement channels based on a standard four-probe configuration, ensuring that the current aligned parallel and the magnetic field maintained perpendicular to the *ab*-plane of each crystal sample. Fig. 4a and b show that the resistivity decreases monotonously while cooling from 300 K to 2 K, indicating a metallic behavior in both $CrHf_xTe_2$ crystals. As illustrated in Fig. S4 (SI), the resistivity at cryogenic temperatures can be fitted with the equation for Fermi liquids: $\rho(T) = \rho_0 + AT^2$. This result implies that the electron–electron scattering occupies a prominent position under cryogenic conditions.

Magnetoresistance (MR) was evaluated at 2 K and 10 K, with the exerted magnetic field aligning vertically to the *ab*-plane. Based on the field-dependent resistivity, magnetoresistance was quantitatively determined using the following formula: MR = $(R_H - R_0)/R_0 \times 100\%$. Fig. 4c and d reveals intrinsic negative magnetoresistances (nMR) that enlarge monotonously with increasing field in the $CrHf_xTe_2$ systems. As the Hf concentration increases from 0.1 to 1/3, the resistivity of $CrHf_xTe_2$ at 2 K reduces from 1.4×10^{-3} to 1.5×10^{-4} Ω cm and simultaneously the nMR maximum rises from −3.8% to −4.7%. The larger nMR of $CrHf_{1/3}Te_2$ is possibly attributed to less electron scattering and enhanced carrier mobility. Such an nMR phenomenon was also discovered in ferromagnetic $Cr_{1.2}Te_2$, $Cr_2Ge_2Te_6$, and anti-ferromagnetic $FeNbTe_2$.[19,35,36] For ferromagnetic crystals, the negative magnetoresistance probably arises from the ordering of the magnetic moments and spin-dependent electron scattering.[35,37] With no external magnetic field, $CrHf_xTe_2$ has a large number of magnetic domains and disorganized magnetic moments. Electrons encounter localized magnetic moments along various directions during transport and experience strong spin scattering, leading to an increase in resistivity. When a sufficiently strong magnetic field is applied, magnetic moments are highly ordered and the spin scattering of electrons is significantly suppressed. Such a robust field also reduces the number of domain walls and the probability of electron scattering is minimized to a great extent. As a result, the nMR effect occurs in the whole field range. However, this characteristic is in contrast to $CrTe_2$: The MR curves exhibit humps (positive MR under low magnetic field) at 2 K, which originates from the spin-reorientation.[37] During the spin-reorientation process, the noncoplanar spin state strengthens the spin scattering of electrons, resulting in positive MR under low field conditions.[35] To sum up, the intrinsic nMR performance in $CrHf_xTe_2$ makes it promising for magnetic sensors, electromagnetic protection and electronic information storage devices.

Conclusion

In summary, a novel intercalation crystal has been successfully synthesized, designated as $CrHf_xTe_2$. $CrHf_{0.1}Te_2$ is characterized with [$CrTe_6$] octahedral coordination and a trigonal crystal structure. The hysteresis loops illustrate ferromagnetic behaviors in $CrHf_xTe_2$, and the easy magnetization direction remains parallel to the *c*-axis. $CrHf_{0.1}Te_2$ displays higher Curie temperature and coercivity than multiple Cr-based vdW ferromagnetic materials like CrI_3, $Cr_2Ge_2Te_6$ and Cr_5Te_8. In addition, the maximum magnetic entropy variation of $CrHf_{0.1}Te_2$ attains 2.85 J kg^{-1} K at about 185 K, and the RCP value (216.6 J kg^{-1}) exceeds that of various vdW ferromagnets. The intrinsic negative magnetoresistance in both $CrHf_xTe_2$ crystals makes them suitable for magnetic sensors. This work provides a promising approach for synthesizing new intercalation compounds with unique properties for advanced electronic and magnetic functions.

Experimental section

Synthesis of $CrHf_xTe_2$ crystals

Both $CrHf_{0.1}Te_2$ and $CrHf_{1/3}Te_2$ were synthesized *via* the flux method, using CsI as the flux agent. Firstly, Cr (Adamas-beta,

99.9%), Hf (Adamas-beta, 99.9%), and Te (Adamas-beta, 99.9%) powders were uniformly mixed in a molar ratio of $1:x:2$ with anhydrous CsI (Innochem, 99.9%). All mixed raw materials and flux were then sealed in evacuated silica tubes by oxyhydrogen flame. Sealed silica tubes were placed in a muffle furnace, which was heated up to 1473 K at a rate of 2 K min^{-1}, equilibrated for two days, and then slowly cooled for three days to 1173 K. The production in silica tubes was finally washed with deionized water to remove the remnants of CsI flux.

Structure characterizations and analyses

Powder X-ray diffraction (PXRD) patterns were obtained through a Bruker D8QUEST diffractometer (Cu Kα radiation). Single-crystal X-ray diffraction (SC-XRD) data were collected on a Bruker D8QUEST diffractometer (Mo Kα radiation), and the crystal structure refinement was analyzed through the APEX3 program. The elemental composition was determined by energy-dispersive X-ray spectroscopy (EDS) coupled with a JEOL (JSM6510) scanning electron microscope (SEM). Chemical valences were analyzed through X-ray photoelectron spectroscopy (XPS). Raman spectra were obtained through a Jobin-Yvon LabRAM HR-800 spectrometer with a laser of 532 nm excitation wavelength.

Electrical transport and magnetic susceptibility measurements

Electrical resistivity and magnetoresistance were tested in a physical property measurement system (PPMS, Quantum Design). Temperature-dependent and field-dependent magnetization characteristics were examined in the VSM module of the PPMS, with external magnetic fields parallel to the *ab*-plane or the *c*-axis of each crystal flake.

Author contributions

Kunqi Li: writing, data assessment, investigation, formal analysis. Xueyang Tu & Xuzhou Sun: software, formal analysis. Hui Bi: writing – review & editing. Yuqiang Fang: writing – review & editing, supervision. Fuqiang Huang: conceptualization, funding acquisition, writing – review & editing, supervision.

Conflicts of interest

There are no conflicts to declare.

Data availability

The data supporting this work are available within the article and the SI. See DOI: **https://doi.org/10.1039/d5tc02160j**

Acknowledgements

This work was financially supported by the Shanghai Rising-Star Program (23QA1410700), Science and Technology Commission of Shanghai Municipality (Grant no. 24LZ1401000), National Natural Science Foundation of China (Grants no. 12104307, no. 12174062, and no. 12241402), Innovation Program for Quantum Science and Technology (2024ZD0300102) and the Program of Shanghai Academic Research Leader (22XD1424300).

Notes and references

1 J. Yang, X. Wang, S. Li, X. Wang, M. Pan, M. Ai, H. Yuan, X. Peng, R. Wang, Q. Li, F. Zheng and P. Zhang, *ACS Nano*, 2023, **17**, 23160–23168.
2 S. N. Kajale, J. Hanna, K. Jang and D. Sarkar, *Nano Res.*, 2024, **17**, 743–762.
3 C. Dai, P. He, L. Luo, P. Zhan, B. Guan and J. Zheng, *Sci. China Mater.*, 2023, **66**, 859–876.
4 B. Wang, X. Liu, F. Hu, J.-T. Wang, J. Xiang, P. Sun, J. Wang, J. Sun, T. Zhao, Z. Mo, J. Shen, Y. Chen, Q. Huang and B. Shen, *J. Am. Chem. Soc.*, 2024, **146**, 35016–35022.
5 Z. Wang, I. Gutiérrez-Lezama, N. Ubrig, M. Kroner, M. Gibertini, T. Taniguchi, K. Watanabe, A. Imamoğlu, E. Giannini and A. F. Morpurgo, *Nat. Commun.*, 2018, **9**, 2516.
6 M. Akram, H. LaBollita, D. Dey, J. Kapeghian, O. Erten and A. S. Botana, *Nano Lett.*, 2021, **21**, 6633–6639.
7 M. Huang, S. Wang, Z. Wang, P. Liu, J. Xiang, C. Feng, X. Wang, Z. Zhang, Z. Wen, H. Xu, G. Yu, Y. Lu, W. Zhao, S. A. Yang, D. Hou and B. Xiang, *ACS Nano*, 2021, **15**, 9759–9763.
8 X. Sun, W. Li, X. Wang, Q. Sui, T. Zhang, Z. Wang, L. Liu, D. Li, S. Feng, S. Zhong, H. Wang, V. Bouchiat, M. Nunez Regueiro, N. Rougemaille, J. Coraux, A. Purbawati, A. Hadj-Azzem, Z. Wang, B. Dong, X. Wu, T. Yang, G. Yu, B. Wang, Z. Han, X. Han and Z. Zhang, *Nano Res.*, 2020, **13**, 3358–3363.
9 S. Husremović, C. K. Groschner, K. Inzani, I. M. Craig, K. C. Bustillo, P. Ercius, N. P. Kazmierczak, J. Syndikus, M. Van Winkle, S. Aloni, T. Taniguchi, K. Watanabe, S. M. Griffin and D. K. Bediako, *J. Am. Chem. Soc.*, 2022, **144**, 12167–12176.
10 C. Zhang, J. Zhang, C. Liu, S. Zhang, Y. Yuan, P. Li, Y. Wen, Z. Jiang, B. Zhou, Y. Lei, D. Zheng, C. Song, Z. Hou, W. Mi, U. Schwingenschlögl, A. Manchon, Z. Q. Qiu, H. N. Alshareef, Y. Peng and X. X. Zhang, *Adv. Mater.*, 2021, **33**, 2101131.
11 C. Bigi, C. Jego, V. Polewczyk, A. De Vita, T. Jaouen, H. C. Tchouekem, F. Bertran, P. Le Fèvre, P. Turban, J.-F. Jacquot, J. A. Miwa, O. J. Clark, A. Jana, S. K. Chaluvadi, P. Orgiani, M. Cuoco, M. Leandersson, T. Balasubramanian, T. Olsen, Y. Hwang, M. Jamet and F. Mazzola, *Nat. Commun.*, 2025, **16**, 4495.
12 Y. Fang, K. Yang, E. Zhang, S. Liu, Z. Jia, Y. Zhang, H. Wu, F. Xiu and F. Huang, *Adv. Mater.*, 2022, **34**, 2200145.
13 D. Zanders, E. Ciftyurek, E. Subaşı, N. Huster, C. Bock, A. Kostka, D. Rogalla, K. Schierbaum and A. Devi, *ACS Appl. Mater. Interfaces*, 2019, **11**, 28407–28422.
14 Y. Peng, X. Cheng, P. Gu, F. Wang, J. Yang, M. Xue, W. Yang, C. Wang, S. Liu, K. Watanabe, T. Taniguchi, Y. Ye and J. Yang, *Adv. Funct. Mater.*, 2020, **30**, 1910036.
15 C.-K. Tian, C. Wang, W. Ji, J.-C. Wang, T.-L. Xia, L. Wang, J.-J. Liu, H.-X. Zhang and P. Cheng, *Phys. Rev. B*, 2019, **99**, 184428.

16 T. V. Chandrasekhar Rao, P. Raj, S. M. Yusur, L. M. Rao, A. Sathyamoorthy and V. C. Sahni, *Philos. Mag. B*, 1996, **74**, 275–291.
17 B. Huang, G. Clark, E. Navarro-Moratalla, D. R. Klein, R. Cheng, K. L. Seyler, D. Zhong, E. Schmidgall, M. A. McGuire, D. H. Cobden, W. Yao, D. Xiao, P. Jarillo-Herrero and X. Xu, *Nature*, 2017, **546**, 270–273.
18 Y. Liu, L. Wu, X. Tong, J. Li, J. Tao, Y. Zhu and C. Petrovic, *Sci. Rep.*, 2019, **9**, 13233.
19 W. Zhuo, B. Lei, S. Wu, F. Yu, C. Zhu, J. Cui, Z. Sun, D. Ma, M. Shi, H. Wang, W. Wang, T. Wu, J. Ying, S. Wu, Z. Wang and X. Chen, *Adv. Mater.*, 2021, **33**, 2008586.
20 A. Wang, Z. Du, F. Meng, A. Rahman, W. Liu, J. Fan, C. Ma, L. Ling, C. Xi, M. Ge, L. Pi, Y. Zhang and L. Zhang, *Phys. Rev. Appl.*, 2024, **22**, 034006.
21 C. Chen, X. Chen, C. Wu, X. Wang, Y. Ping, X. Wei, X. Zhou, J. Lu, L. Zhu, J. Zhou, T. Zhai, J. Han and H. Xu, *Adv. Mater.*, 2022, **34**, 2107512.
22 X. Zhang, T. Yu, Q. Xue, M. Lei and R. Jiao, *J. Alloy. Compd.*, 2018, **750**, 798–803.
23 D. Ghazaryan, M. T. Greenaway, Z. Wang, V. H. Guarochico-Moreira, I. J. Vera-Marun, J. Yin, Y. Liao, S. V. Morozov, O. Kristanovski, A. I. Lichtenstein, M. I. Katsnelson, F. Withers, A. Mishchenko, L. Eaves, A. K. Geim, K. S. Novoselov and A. Misra, *Nat. Electron.*, 2018, **1**, 344–349.
24 S. Yang, X. Xu, B. Han, P. Gu, R. Guzman, Y. Song, Z. Lin, P. Gao, W. Zhou, J. Yang, Z. Chen and Y. Ye, *J. Am. Chem. Soc.*, 2023, **145**, 28184–28190.
25 A. Goswami, N. Ng, A. M. M. Abeykoon, E. Yakubu and S. Guchhait, *ACS Appl. Electron. Mater.*, 2024, **6**, 4043–4056.
26 Y.-D. Wu, W.-W. Duan, Q.-Y. Li, W. Geng, C. Zhang, Q.-Q. Lv, L. He, J.-Q. Chen, X.-Y. Hu, Y.-L. Qin, Y. Meng, Y. Ma, L.-Y. Liu, X.-H. Ma and Z.-F. Zi, *J. Alloy. Compd.*, 2022, **894**, 162447.
27 X. Zhao, X. Zheng, X. Luo, F. Gao, H. Zeng, G. Yu, S. U. Rehman, C. Chen, S. Ma, W. Ren and Z. Zhong, *J. Mater. Sci. Technol.*, 2021, **86**, 56–63.
28 D. Wang, X. Zheng, L. He, H. Wu, Y. Gao, G. Wang, H. Liu, S. Zhen, Y. Pan, Z. Zhang, G. Zhang, A. Ma, Z. Chen, L. Xi, J. Xu, S. Wang and B. Shen, *Mater. Today Phys.*, 2025, **50**, 101609.
29 H. Xie, X. Lv, Z. Mo, J. Gong, X. Gao, Z. Li, J. Wu and J. Shen, *J. Mater. Sci. Technol.*, 2024, **193**, 90–97.
30 H. B. Tran, H. Momida, Y.-I. Matsushita, K. Shirai and T. Oguchi, *Acta Mater.*, 2022, **231**, 117851.
31 Y. Sun and X. Luo, *Phys. Status Solidi B*, 2019, **256**, 1900052.
32 Y. Liu, J. Li, J. Tao, Y. Zhu and C. Petrovic, *Sci. Rep.*, 2019, **9**, 13233.
33 Y. Liu, M. Abeykoon and C. Petrovic, *Phys. Rev. Res.*, 2020, **2**, 013013.
34 S. Pandey and S. Mukhopadhyay, *Phys. Rev. B*, 2024, **110**, L060405.
35 M. Huang, L. Gao, Y. Zhang, X. Lei, G. Hu, J. Xiang, H. Zeng, X. Fu, Z. Zhang, G. Chai, Y. Peng, Y. Lu, H. Du, G. Chen, J. Zang and B. Xiang, *Nano Lett.*, 2021, **21**, 4280–4286.
36 W. Bai, Z. Hu, S. Wang, Y. Hua, Z. Sun, C. Xiao and Y. Xie, *Adv. Mater.*, 2019, **31**, 1900246.
37 L. Meng, Z. Zhou, M. Xu, S. Yang, K. Si, L. Liu, X. Wang, H. Jiang, B. Li, P. Qin, P. Zhang, J. Wang, Z. Liu, P. Tang, Y. Ye, W. Zhou, L. Bao, H.-J. Gao and Y. Gong, *Nat. Commun.*, 2021, **12**, 809.